

RAW-Diffusion: RGB-Guided Diffusion Models for High-Fidelity RAW Image Generation

Christoph Reinders^{1†} Radu Berdan^{2*} Beril Besbinar^{2*} Junji Otsuka³ Daisuke Iso²
¹Leibniz University Hannover ²Sony AI ³Sony Group Corporation

Abstract

Current deep learning approaches in computer vision primarily focus on RGB data sacrificing information. In contrast, RAW images offer richer representation, which is crucial for precise recognition, particularly in challenging conditions like low-light environments. The resultant demand for comprehensive RAW image datasets contrasts with the labor-intensive process of creating specific datasets for individual sensors. To address this, we propose a novel diffusion-based method for generating RAW images guided by RGB images. Our approach integrates an RGB-guidance module for feature extraction from RGB inputs, then incorporates these features into the reverse diffusion process with RGB-guided residual blocks across various resolutions. This approach yields high-fidelity RAW images, enabling the creation of camera-specific RAW datasets. Our RGB2RAW experiments on four DSLR datasets demonstrate state-of-the-art performance. Moreover, RAW-Diffusion demonstrates exceptional data efficiency, achieving remarkable performance with as few as 25 training samples or even fewer. We extend our method to create BDD100K-RAW and Cityscapes-RAW datasets, revealing its effectiveness for object detection in RAW imagery, significantly reducing the amount of required RAW images. The code is available at <https://github.com/SonyResearch/RAW-Diffusion>.

1. Introduction

In the traditional imaging pipeline, a camera sensor captures a RAW image, which is then converted via an Image Signal Processor (ISP) and compressed to a RGB image tailored for human consumption. However, while RGB images are convenient for human perception and readily available, their processing from RAW format introduces artifacts and information loss. Nonetheless, RGB images are ubiquitous in contemporary computer vision applications and

[†] Work done during an internship at Sony AI. Corresponding author: reinders@tnt.uni-hannover.de

^{*} These authors contributed equally to this work

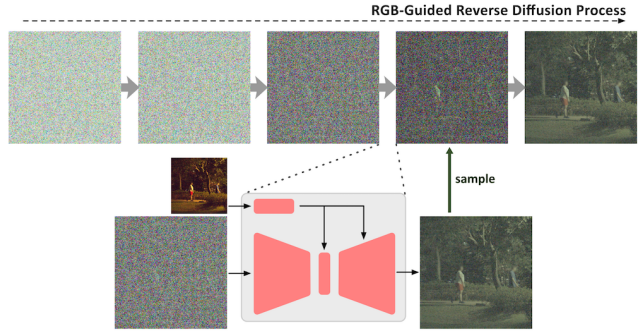


Figure 1. RAW-Diffusion enables the generation of high-fidelity RAW images by iterative denoising of a noisy RAW input through a RGB-guidance module and RGB-guided residual blocks. RAW-Diffusion is the first successful diffusion-based method for RAW generation that outperforms state-of-the-art methods.

serve as the primary data source for training neural networks. When running large computer vision models in the cloud, performing inference on RGB images is advantageous for reasons other than model performance: they are more cost-effective to transmit and store than their original RAW images. On the other hand, when running CV models on the edge, under strict resource and hardware constraints, extracting the maximum information from the scene and avoiding unnecessary pre-processing in order to maximize small model performance becomes critical.

The limitations of RGB images are particularly evident in scenarios requiring precise scene irradiance information, such as low-light environments or fine-grained image manipulation tasks. In contrast, RAW images captured directly by camera sensors offer a more faithful representation of scene data, retaining higher quantization levels and preserving the unprocessed sensor readings. The enhanced dynamic range of RAW images has demonstrated superior performance for a variety of image editing and computer vision tasks, including photometric stereo [76], denoising [1, 3, 26], reflection removal [41], low-light image enhancement [16], image super-resolution [98], and object detection [63]. Employing RAW image inputs can thus improve the accuracy and robustness of neural networks

across various computer vision tasks [5], especially when running on the edge. However, sensor-specific data collection and annotation for RAW datasets is extremely costly. Moreover, accessing RAW images can be challenging due to their memory-intensive nature, posing difficulties in storage, transfer, and sharing.

To address this issue, several approaches have been proposed to map RGB images to corresponding RAW sensor outputs [2, 9, 13, 28, 28, 38, 45, 57, 89, 95], some relying on metadata or prior camera information for reverse ISP reconstruction [3, 18, 28, 45, 57], which is not always accessible. Recent approaches aim to learn invertible functions for mapping between RGB and RAW images, achieving superior RAW synthesis performance. Among those, many methods [43, 49, 91] mimic traditional ISP pipelines, requiring sensor-specific configurations but being more data efficient. Others [3, 89, 95] learn nonlinear mappings using RGB-RAW image pairs, often requiring many training samples. Our goal is to develop a flexible, data-efficient, and high-performing method for RAW image synthesis.

In this work, we present a novel diffusion model for RAW image reconstruction, employing features derived from an RGB image (see Fig. 1). Unlike conventional methods that simply concatenate or add guidance signals [52], we introduce RGB-guided residual blocks for integrating RGB features and guiding the denoising of the RAW images. This approach not only achieves state-of-the-art performance in RAW image reconstruction but also facilitates a data-efficient method for generating large-scale sensor-specific datasets using existing RGB images. In summary, our **contributions** are as follows:

- We propose a novel diffusion model for accurate RAW image reconstruction with RGB image guidance.
- The proposed method demonstrates superior performance in RAW image synthesis with high-bit sensors, especially for images featuring challenging irradiance distributions, and surpasses state-of-the-art methods.
- Our method is extremely data-efficient, achieving the same performance with 25 or fewer training samples as when training on the full training set.
- We enable the creation of camera-specific RAW datasets from existing RGB datasets, eliminating the need for costly sensor-specific data acquisition.
- The proposed method bridges the gap between models trained on RGB images for downstream tasks and RAW images, as shown for object detection.

2. Related Work

RAW Image Reconstruction. Unmapping the processed RGB images back to the RAW domain has been a long-standing research topic. Conventional radiometric calibration

algorithms use multiple images taken with controlled exposures to compute the response function of a camera’s output intensity values with respect to the amount of light falling on the sensor [18, 28, 45, 57], which are further advanced to handle saturated RGB values [9, 10, 38]. However, these methods require calibration for a given camera, which involves multiple parameterized models for different camera settings. Modern deep learning-based algorithms [2, 3, 12, 13, 26, 43, 49, 49, 74, 89, 95] have shown how data-driven approaches can outperform conventional methods without the heavy need for calibration. These methods either replace each or groups of ISP elements with neural networks [43, 49, 91] or model RGB-to-RAW or RAW-to-RGB mapping with a single network [3, 89, 95]. While being more data efficient, the first approach requires sensor-specific configuration. In contrast, the single network approach requires large datasets of RGB-RAW image pairs.

Diffusion Models. Diffusion models [32], a probabilistic generative approach, have recently gained prominence for their ability to produce high-quality images with diverse features. They operate through a forward process, adding noise to clean samples, and a reverse process, recovering samples from noise [15, 56]. Offering stable training and strong priors compared to other generative models like GANs and VAEs [32], these models excel in various tasks like image generation [19, 33, 61, 66, 73], inpainting [55, 88], molecular generation [90], audio synthesis [39], and medical image analysis [37]. Denoising diffusion probabilistic models (DDPMs) [32], primarily focus on removing noise from images, while Denoising Diffusion Implicit Models (DDIMs) [78] generalize DDPMs in a more computationally efficient inference scheme via a non-Markovian forward process. As a generative model, they show the potential for enhancing datasets to improve downstream tasks like image classification [81] or object detection [25].

Object detection. Deep learning methods have demonstrated remarkable performance across various domains of computer vision [7, 22, 29, 30, 40, 62, 70, 71, 96], including significant improvements in object detection through data-driven approaches [8, 50, 67–69, 72, 100]. Object detection methods are generally classified into two categories: single-stage [47, 51, 67, 75, 79, 80] and two-stage methods approaches [27, 46, 72]. Notably, models like the YOLO [67] family and Faster R-CNN [72] have been widely adopted as representative approaches. Recently, there has been a growing interest in leveraging RAW images for object detection [5, 35, 53, 58, 91, 92], as they offer more precise information, particularly beneficial in low-light environments [35].

3. Method

The proposed diffusion-based method is able to iteratively generate high-fidelity RAW images, simulate the distribution of the camera sensor, and create specific scenes by injecting RGB-guidance at multiple resolutions with RGB-guidance residual blocks into the diffusion process. In the following, we will briefly present the foundations of DDPMs. Afterward, the RGB-guidance module is introduced, which is followed by the architecture of the diffusion model including the conditional image generation. Finally, the training objective of the diffusion model is presented.

3.1. Preliminaries

Diffusion models [32, 77] are latent variable generative models inspired by non-equilibrium thermodynamics. In the forward diffusion process, a Markov chain of T steps is formulated by gradually adding random noise to the data. Given a data sample from the real data distribution $x_0 \sim q(x)$, a sequence of latent variables x_1, \dots, x_T is generated by progressively adding Gaussian noise:

$$q(x_t | x_{t-1}) = \mathcal{N}(x_t; \sqrt{1 - \beta_t}x_{t-1}, \beta_t I), \quad (1)$$

where $0 < \beta_t < 1$ is the variance schedule of the Gaussian noise, and I the identity matrix. By defining $\alpha_t = 1 - \beta_t$ and $\bar{\alpha}_t = \prod_{i=1}^t \alpha_i$, x_t can be sampled at an arbitrary time step in closed form using the reparametrization trick $x_t = \sqrt{\bar{\alpha}_t}x_0 + \sqrt{1 - \bar{\alpha}_t}\epsilon$ with $\epsilon \in \mathcal{N}(0, I)$, i.e., $q(x_t | x_0) = \mathcal{N}(x_t; \sqrt{\bar{\alpha}_t}x_0, \sqrt{1 - \bar{\alpha}_t}I)$.

The reverse diffusion process is learned by training a parameterized model p_θ to recover the data and gradually remove noise. Starting from random noise $x_T \sim \mathcal{N}(0, I)$, the distribution of x_{t-1} given x_t and t is modeled as

$$p_\theta(x_{t-1} | x_t) = \mathcal{N}(x_{t-1}; \mu_\theta(x_t, t), \sigma_t^2 I) \quad (2)$$

to generate new data samples, where μ_θ is the Gaussian mean estimated by the denoising network and σ_t is a fixed variance.

3.2. RAW-Diffusion

RAW-Diffusion is based on DDPMs and learns the reconstruction of a RAW image by starting from random noise and iterative denoising of a noisy RAW image guided by an RGB image. We introduce an RGB-guidance module that extracts features from the RGB images. The diffusion model, utilizing a U-Net architecture, injects the features into the diffusion process to guide the generation, and directly predicts the RAW image, without ϵ -prediction. An overview of RAW-Diffusion is shown in Fig. 2 and the individual components are introduced in the following sections.

3.2.1 RGB-Guidance Module

For high-fidelity RAW image synthesis, the guidance features from the ISP-processed RGB image $I_{\text{RGB}} \in$

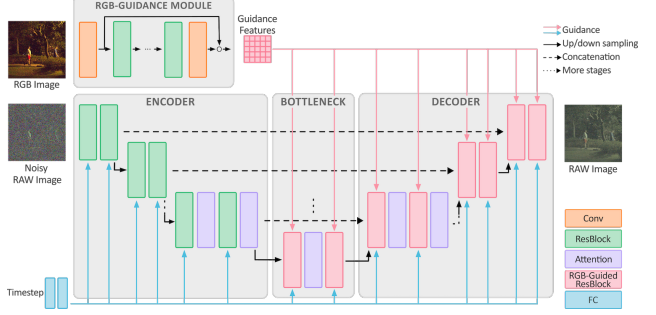


Figure 2. The RAW-Diffusion architecture consists of an RGB-guidance module for creating guidance features and an encoder for processing noisy RAW inputs. The guidance features are then integrated into both the bottleneck and decoder with RGB-guidance residual blocks, modulating the diffusion features to reconstruct the RAW image.

$\mathcal{R}^{3 \times H \times W}$ should contain both low- and high-level information. Hence, we propose using the enhanced deep super-resolution network (EDSR) [44] without an upsampling head for feature extraction. The RGB image I_{RGB} is first processed by a convolutional layer to lift the RGB channels to $C_{\text{GM,Features}}$ channels, which are later fed to a sequence of $N_{\text{GM,ResBlocks}}$ residual blocks. Each residual block consists of two convolutional layers followed by ReLU activation and a skip connection. The output of the residual blocks is then added to the initial convolved features, resulting in a feature map $F_{\text{RGB}} \in \mathcal{R}^{C \times H \times W}$, where $C = C_{\text{GM,Features}}$. All convolutional layers employ 3×3 kernels with reflective padding of size 1, and the guidance module does not contain any normalization layers based on empirical results.

3.2.2 Encoder

The encoder network follows a standard architecture [20] and derives a multi-scale feature representation of the noisy RAW image. The input at each level is processed by $N_{\text{ResBlocks}}$ residual blocks, followed by a downsampling layer that halves the spatial resolution, while expanding the feature dimension. Each residual block is characterized by two convolutional layers, each followed by SiLU activation [24, 31, 65] and group normalization [86]. The current timestep t of the diffusion process is mapped to a learnable embedding that is later projected onto a set of affine parameters for channel-specific transformation of the encoder features after the second group normalization. We also employ self-attention blocks after each residual block at specific resolutions to facilitate learning long-term dependencies between different spatial regions.

3.2.3 RGB-Guided Residual Block

Our objective is the guidance of the diffusion process for reconstructing RAW images using the relevant RGB infor-

mation. For an overview of the fundamentals of guiding diffusion models, please refer to [34, 59, 97]. A naive solution involves concatenating the additional information directly with the noisy input. However, we introduce an RGB-guided residual block to inject RGB information into the network, enhancing the RAW image reconstruction. For that, we integrate the RGB-guidance features by modulating the feature transformation within the residual block. The RGB-guided residual block is inspired by the semantic diffusion model [83] which uses spatially-adaptive normalization (SPADE) [64] to condition the diffusion process. We introduce two layer-specific modules γ^i and β^i which downscale the RGB guidance features by bilinear interpolation and predict modulation parameters $\gamma^i(x) \in \mathcal{R}^{C \times H' \times W'}$ and $\beta^i(x) \in \mathcal{R}^{C \times H' \times W'}$ for each feature and spatial position, where $H' \times W'$ is the size of the feature map and C number of channels. The modules γ^i and β^i consist of a shared convolutional layer with ReLU activation followed by another individual convolutional layer. Afterward, the RGB information is integrated by scaling and shifting the normalized diffusion features F^i as follows:

$$F^{i+1} = \text{Norm}(F^i) \cdot (1 + \gamma^i(\text{Down}(F_{\text{RGB}}))) + \beta^i(\text{Down}(F_{\text{RGB}})). \quad (3)$$

The RGB-guided spatially adaptive normalization envelops both instances of group normalization within each residual block, learning to incorporate the relevant RGB information across multiple resolutions to guide the RAW image reconstruction process effectively.

3.2.4 Bottleneck

Starting with the bottleneck, we inject the RGB-guidance features into the diffusion process by modulating the high-level diffusion features with the proposed RGB-guided residual block. The bottleneck is composed of an RGB-guided ResBlock, an attention block, and another RGB-guided ResBlock.

3.2.5 Decoder

The decoder, symmetric to the encoder, takes the concatenation of the upscaled features from the preceding level and the shortcut connection from the encoder as input at each layer. Each decoder level is composed of a series of RGB-guided residual blocks and attention blocks. The final level decoder features are then projected via a convolutional layer and a hyperbolic tangent function to compose the RAW image. Our method directly predicts the denoised RAW image rather than estimating noise.

3.3. Training Objective

The diffusion model is trained with pairs of RAW and RGB images, denoted as I_{RAW} and I_{RGB} . In each training step, noisy RAW images and RGB images are provided as

input, and the model is optimized to directly predict the RAW image \hat{I}_{RAW} . We define three loss functions to facilitate the accurate reconstruction of the original RAW image. First, the squared difference and mean absolute difference are optimized via \mathcal{L}_{MSE} and \mathcal{L}_{L1} , respectively. In addition, to address the bias in the distribution of the RAW pixel values towards low values, a logarithmic L1 loss [23], defined as $\mathcal{L}_{\log\text{L1}}(\hat{I}, I) = \frac{1}{C \cdot H \cdot W} \|\log(\hat{I} + \epsilon) - \log(I + \epsilon)\|_1$, where ϵ serves as a minimal constant to ensure numerical stability, is adopted. For the $\mathcal{L}_{\log\text{L1}}$, the value range is adjusted to $[0, 1]$. Hence, the overall training objective is defined as the composition of all three losses: $\mathcal{L} = \mathcal{L}_{\text{MSE}} + \mathcal{L}_{\text{L1}} + \mathcal{L}_{\log\text{L1}}$.

4. Experiments

We perform extensive experiments to evaluate the performance of RAW-Diffusion and state-of-the-art methods.

4.1. Datasets

The experiments are performed on diverse image sets captured by four different DSLR cameras, two from each the MIT-Adobe FiveK [6] and NOD datasets [58]. Following [89], we use 777 and 590 images captured by the Canon EOS 5D camera and Nikon D700 cameras, respectively, and use a train-test split of 85/15. The Night Object Detection (NOD) dataset [58] consists of RAW images recorded by Sony RX100 VII and Nikon D750, with object annotations of three classes. The Sony camera has 3.2k images with 18.7k annotated instances, and Nikon has 4.0k with 28.0k annotated instances. We use the official training and test split. All RAW images are processed using the RawPy library to generate the corresponding RGB image. Additionally, we integrate two large-scale RGB datasets: Cityscapes [14] and BDD100K [93] (denoted as CS and BDD). Cityscapes consists of 5,000 images with pixel-level instance segmentation annotations recorded in street scenes from 50 different cities. BDD100K is a diverse dataset with 100k videos and various tasks. The dataset provides object detection annotations for 100k keyframes.

4.2. Experimental Setup

Training Details. We normalize the data to the range $[-1, 1]$. The RAW images are scaled based on the black and white level. During training, patches of size 256×256 are sampled by using random cropping, rotation, and flipping augmentation. RAW-Diffusion is trained for 70k steps using AdamW [54] with an initial learning rate of 0.0001, no weight decay, and a batch size of 4. The learning rate is decreased linearly to zero. Following [60], the number of diffusion steps, T , is set to 1000, and a linear variance schedule is used ranging from $\beta_1 = 0.0001$ to $\beta_T = 0.02$. For object detection, Faster R-CNN [72] and YOLOv8 [36] models are trained. Details and other hyper-parameters are provided in the supplementary material. All trainings are conducted on

Table 1. Quantitative RGB2RAW results on the test set of four DSLR cameras evaluating the RAW reconstruction performance using PSNR (\uparrow) and SSIM (\uparrow) of various state-of-the-art methods and RAW-Diffusion. We report the mean performance and standard deviation. The best result is highlighted in bold, and the second best underlined.

Method	FiveK Nikon		FiveK Canon		NOD Nikon		NOD Sony	
	PSNR	SSIM	PSNR	SSIM	PSNR	SSIM	PSNR	SSIM
U-Net [13]	26.00 \pm 1.02	0.507 \pm 0.06	27.77 \pm 2.23	0.691 \pm 0.09	37.90 \pm 2.19	0.791 \pm 0.10	37.71 \pm 0.30	0.813 \pm 0.02
UPI [4]	27.66 \pm 0.03	0.830 \pm 0.00	30.68 \pm 0.08	0.893 \pm 0.00	37.12 \pm 0.05	0.816 \pm 0.00	33.49 \pm 0.02	0.735 \pm 0.00
InvGrayscale [87]	28.32 \pm 0.55	0.838 \pm 0.01	29.67 \pm 0.43	0.884 \pm 0.00	30.41 \pm 0.38	0.803 \pm 0.01	29.52 \pm 0.42	0.756 \pm 0.00
InvISP [89]	26.41 \pm 0.19	0.732 \pm 0.01	30.26 \pm 0.42	0.885 \pm 0.00	32.50 \pm 1.91	0.844 \pm 0.05	23.35 \pm 3.50	0.533 \pm 0.11
InvISP ⁺ [89]	28.95 \pm 0.15	0.841 \pm 0.00	<u>32.23</u> \pm 0.09	<u>0.912</u> \pm 0.00	<u>42.57</u> \pm 0.09	<u>0.973</u> \pm 0.00	38.27 \pm 0.01	0.916 \pm 0.00
ISPLess [17]	26.82 \pm 0.15	0.762 \pm 0.02	29.73 \pm 1.44	0.880 \pm 0.01	33.04 \pm 0.71	0.870 \pm 0.02	29.66 \pm 0.39	0.669 \pm 0.03
ISPLess ⁺ [17]	<u>29.83</u> \pm 0.41	<u>0.845</u> \pm 0.00	32.15 \pm 0.25	0.904 \pm 0.00	41.50 \pm 0.02	0.967 \pm 0.00	38.31 \pm 0.07	<u>0.917</u> \pm 0.00
CycleR2R [42]	28.40 \pm 0.85	0.842 \pm 0.01	24.85 \pm 3.45	0.791 \pm 0.05	24.93 \pm 1.86	0.562 \pm 0.03	23.71 \pm 1.4	0.491 \pm 0.02
RISPNet [21]	29.00 \pm NA	0.669 \pm NA	29.56 \pm NA	0.789 \pm NA	40.07 \pm NA	0.898 \pm NA	<u>38.67</u> \pm NA	0.871 \pm NA
Diffusion [52]	27.64 \pm 0.07	0.798 \pm 0.00	29.17 \pm 0.15	0.840 \pm 0.00	35.59 \pm 1.29	0.867 \pm 0.02	33.07 \pm 1.16	0.812 \pm 0.02
SRISP [63]	28.19 \pm 0.15	0.797 \pm 0.00	30.34 \pm 0.27	0.844 \pm 0.00	38.23 \pm 0.85	0.880 \pm 0.01	35.22 \pm 0.76	0.815 \pm 0.01
RAW-Diffusion (ours)	30.05 \pm 0.32	0.857 \pm 0.00	34.01 \pm 0.27	0.926 \pm 0.00	44.93 \pm 0.15	0.983 \pm 0.00	39.17 \pm 0.03	0.932 \pm 0.00

a single NVIDIA Tesla V100 with 16 GB memory, and repeated with three different seeds.

Evaluation. In line with prior works, we evaluate the PSNR and SSIM [85] to assess the quality of the generated RAW images. The images are normalized to the range of [0, 1] for calculating the metrics. Similar to [89], we use a patch-based evaluation on a regular 3×3 grid. The precision of the object detection models is analyzed using the Average Precision (AP) [48].

4.3. RGB2RAW Results

We evaluate the RAW reconstruction performance of our proposed RAW-Diffusion and various state-of-the-art methods such as U-Net [13], UPI [4], InvGrayscale [87], InvISP [89], InvISP⁺ [89], ISPLess [17], ISPLess⁺ [17], CycleR2R [42], RISPNet [21], Diffusion [52], and SRISP [63]. For UPI, the model parameters are optimized using the camera metadata, as described in the paper. It should be noted that we are able to reproduce the InvISP results reported by the authors. However, the official implementation evaluates the inverse pass by rendering the sRGB images through the forward pass of the invertible neural network. Here, we use the same RGB images for all methods. We improve the performance of InvISP and ISPLess by removing the JPEG simulation and training the inverse process with the ground truth RGB image as input, denoted as InvISP⁺ and ISPLess⁺. For RISPNet, we do not perform either model or test-time ensembling. In addition, we perform a single training due to computational requirements despite the downscaled model size. For SRISP, the mean global feature of all training images is used as test-time reference which has proven more effective than sampling a reference. Diffusion is trained on 64×64 patches as described by the authors. The performance with larger patch sizes collapses.

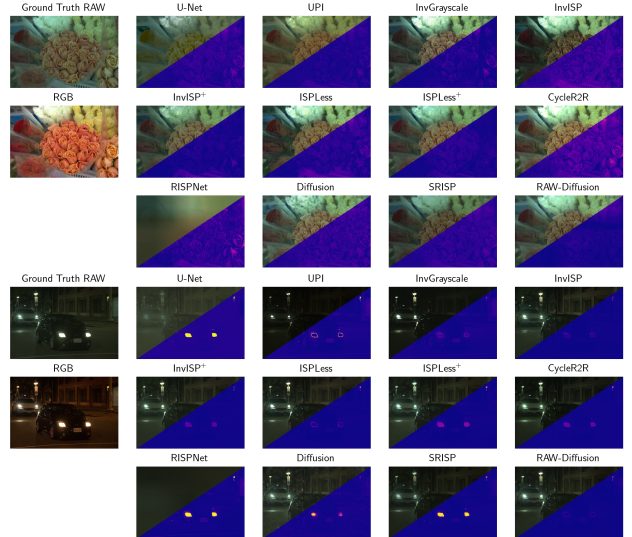


Figure 3. Qualitative results on FiveK (top) and NOD (bottom). The reconstructed RAW image and the error map are presented for each method. The RAW images are shown with a gamma correction of $1/2.2$ for visualization.

The results on the FiveK and NOD test sets for both cameras are shown in Tab. 1. On FiveK Nikon, U-Net records a PSNR of 26.00, while UPI reaches a PSNR of 27.66. ISPLess and ISPLess⁺ achieve a PSNR of 26.82 and 29.83, respectively. RAW-Diffusion attains the highest PSNR of 30.05. On NOD, the variability in results widens due to the challenging conditions of the dataset by the skewed distribution of the RAW values and focus on low-light scenarios across both cameras. CycleR2R demonstrates the lowest performance with 24.93 PSNR on NOD Nikon. InvISP⁺ achieves a PSNR of 42.57 and RAW-Diffusion reaches a PSNR of 44.93. Overall, RAW-Diffusion is able to achieve

Table 2. Results of training RAW-Diffusion with limited training data. Even when trained with only 25 images, RAW-Diffusion achieves the same performance as trained on the full dataset.

Training Images	FiveK Nikon		FiveK Canon		NOD Nikon		NOD Sony	
	PSNR	SSIM	PSNR	SSIM	PSNR	SSIM	PSNR	SSIM
Full	30.05	0.857	34.01	0.926	44.93	0.983	39.17	0.932
500	30.39	0.858	34.41	0.930	44.70	0.983	39.28	0.931
250	30.50	0.861	35.93	0.949	45.11	0.983	39.22	0.933
100	30.80	0.853	36.14	0.948	45.28	0.983	39.27	0.932
50	30.80	0.837	35.32	0.928	45.38	0.982	39.26	0.931
25	31.29	0.850	34.17	0.914	45.51	0.982	39.05	0.929
10	30.54	0.830	33.44	0.893	45.31	0.979	38.66	0.922

the best results across all datasets. Qualitative results for each method are shown in Fig. 3.

4.4. Small Data RGB2RAW Results

Collecting large amounts of RAW images for each RAW camera model is extremely expensive. Therefore, we analyze the performance of RAW-Diffusion when trained with limited data by subsampling the original training set. In the following experiment, we conduct experiments with 500, 250, 100, 50, 25, and 10 training samples for training the diffusion model. To maintain a consistent number of training steps, the small training sets are repeated accordingly. In Tab. 2, the average results on the test set of FiveK and NOD are shown. With only 25 training samples, RAW-Diffusion achieves a PSNR of 31.29 and an SSIM of 0.850 on FiveK Nikon compared to 30.05 and 0.857, respectively, on the full training set. Similarly, the performance remains robust across the other three DSLR datasets, even with the limited sample size. Interestingly, the performance initially slightly improves with smaller portions of the training dataset compared to the full dataset. There are two reasons. First, the training on the full dataset is performed epoch-based while training on the subsampled datasets is iteration-based which improves performance. Additionally, the issue arises from distribution shifts between training and test sets, especially for small datasets. When increasing the number of training runs, the results better align with the expectations. The remaining variance falls within stochastic uncertainty. Overall, performance with limited data is very robust. Training the diffusion model with only 10 samples still yields a consistent performance on FiveK Nikon and NOD Nikon, achieving a PSNR of 30.54 and 45.31. On FiveK Canon and NOD Sony, the PSNR decreases to 33.44 (−0.57) and 38.66 (−0.51), respectively. The experiment reveals that RAW-Diffusion is capable of learning a precise reconstruction with very few training examples.

4.5. Object Detection Results

The goal is to enable the training of neural networks for new camera sensors with very few training examples. Unlike typical labor-intensive data labeling, we generate real-

Table 3. Object detection results using Faster R-CNN evaluating the performance on 100 NOD training samples (RGB and RAW) and the integration of Cityscapes-RAW and BDD100K-RAW generated by SRISP and RAW-Diffusion.

Training Dataset	NOD Nikon			NOD Sony		
	AP	AP ₅₀	AP ₇₅	AP	AP ₅₀	AP ₇₅
RGB	19.1±0.2	36.8±0.4	17.7±0.6	19.2±0.5	38.2±0.8	17.6±0.5
RAW	18.2±0.2	35.3±0.2	17.1±0.2	18.0±0.1	35.8±0.3	16.3±0.4
RAW + CS-RAW (SRISP)	23.0±0.6	43.9±0.4	21.9±1.5	23.1±0.4	46.9±0.4	20.0±0.1
RAW + BDD (SRISP)	24.2±0.3	45.7±0.4	22.6±0.7	26.0±0.2	50.5±0.6	24.2±0.5
RAW + CS-RAW (ours)	24.7±0.3	46.3±0.6	23.9±0.2	26.2±0.3	50.6±0.6	24.9±0.4
RAW + BDD-RAW (ours)	26.5±0.3	49.3±0.5	25.3±0.5	28.6±0.1	55.2±0.4	26.4±0.3

Table 4. Performance on the test set using YOLOv8 for training on NOD and combinations of NOD with generated datasets.

Training Dataset	NOD Nikon			NOD Sony		
	AP	AP ₅₀	AP ₇₅	AP	AP ₅₀	AP ₇₅
RGB	22.7±1.7	32.9±10	22.5±1.8	18.4±0.3	33.8±0.2	18.4±0.4
RAW	25.8±0.5	45.5±0.8	25.7±0.9	27.6±0.4	49.3±0.2	27.0±0.9
RAW + CS-RAW (SRISP)	29.1±0.1	48.6±0.2	29.4±0.1	29.5±0.4	51.7±0.6	29.1±0.7
RAW + BDD-RAW (SRISP)	<u>32.0±0.3</u>	<u>53.1±0.5</u>	<u>32.1±0.4</u>	<u>32.0±0.7</u>	<u>55.3±0.8</u>	<u>31.6±0.8</u>
RAW + CS-RAW (ours)	29.9±0.3	50.2±0.5	30.7±0.7	31.0±0.3	54.8±0.5	31.0±0.5
RAW + BDD-RAW (ours)	32.6±0.1	54.3±0.2	32.6±0.7	33.6±0.1	58.3±0.2	33.8±0.0

istic, sensor-specific RAW images from existing large-scale RGB datasets for training. We evaluate the object recognition performance on NOD (both Nikon and Sony cameras), using 100 NOD images to assess adaptation to new sensors with limited target domain data.

We analyze the integration of Cityscapes [14] and BDD100K [93] as large-scale RGB datasets with a large number of labeled images, and generate Cityscapes-RAW and BDD100K-RAW with SRISP [63], a recent, state-of-the-art RGB2RAW conversion method, and RAW-Diffusion, each for both cameras. Both methods are trained with a limited number of samples from NOD. For RAW-Diffusion, we utilize a sampling process with 24 or 6 sampling steps via DDIM, respectively. The generated datasets are combined with the small original sample collection from NOD by defining a probability p_{gen} . This probability determines the likelihood of selecting a sample from the generated dataset or, from NOD, thereby ensuring the overall number of training steps remains the same.

The results on the test set of NOD Nikon and Sony using Faster R-CNN, a two-stage method, are shown in Tab. 3. Training on the original RGB and RAW images reaches an AP of 19.1 and 18.2, respectively, on NOD Nikon. Incorporating Cityscapes-RAW and BDD100K-RAW, generated by SRISP, enhances the AP to 23.0 and 24.2 AP. The training on the generated datasets by RAW-Diffusion raises the performance to 24.7 and 26.5. Additionally, we perform the evaluation using YOLOv8, a one-stage method. The results in Tab. 4 show a similar outcome, where models trained on both Cityscapes-RAW and BDD100K-RAW datasets generated by our method outperform models trained on the same

Table 5. Zero-shot object detection results using Faster R-CNN. The models are trained exclusively on the generated datasets and evaluated on the NOD test set.

Training Dataset	NOD Nikon			NOD Sony		
	AP	AP ₅₀	AP ₇₅	AP	AP ₅₀	AP ₇₅
CS-Raw (SRISP)	7.7±1.0	16.8±2.7	6.4±0.6	3.8±1.1	9.3±2.8	2.6±0.5
BDD-Raw (SRISP)	18.4±0.3	35.9±0.3	15.8±0.5	16.9±0.6	34.2±0.6	14.5±0.8
CS-Raw (ours)	12.0±0.7	23.4±1.6	11.4±0.5	13.7±1.3	29.4±2.3	11.7±0.8
BDD-Raw (ours)	22.0±0.1	43.1±0.3	18.8±0.5	21.6±0.1	43.7±0.4	18.7±0.2

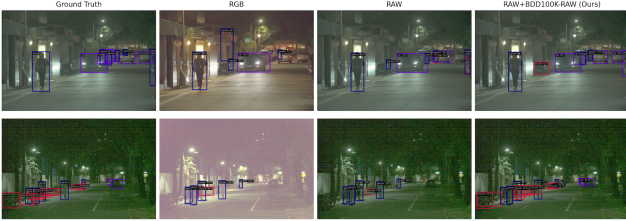


Figure 4. Qualitative results on NOD Nikon (top) and Sony (bottom) for training on the RGB and RAW dataset and a combination with BDD100K-RAW generated by RAW-Diffusion. Please refer to the supplementary material for further qualitative analysis.

datasets converted by SRISP. These results highlight the importance of generating high-fidelity RAW images when converting RGB datasets to a target domain, for increasing performance on a downstream task such as object detection.

In the next experiment, we assess zero-shot performance when training on the generated datasets exclusively (see Tab. 5). While Cityscapes-RAW generated by SRISP achieves an AP of 7.7 and RAW-Diffusion reaches an AP of 12.0, the results indicate that the domain shift from Cityscapes, notably its limitation to daylight images, is too significant for effective training without any NOD images. However, the larger dataset size and greater diversity in BDD100K(-RAW) increase performance, achieving 18.4 for SRISP and 22.0 for RAW-Diffusion. The zero-shot results using YOLO are shown in the supplementary material.

4.6. Analyses and Ablation Studies

We conduct several analyses and ablation studies to examine the fundamental components of the proposed method and assess their impact on the performance.

RAW-Diffusion Architecture. First, we analyze the architecture of the diffusion model. The results in Tab. 6 reveal that predicting the noise, which is a common parametrization in the image domain, does not translate effectively to RAW images, leading to 5.55 PSNR on NOD Nikon. Instead, we achieve significantly better results by directly learning the reconstruction of the RAW image. Furthermore, we explore the effect of the RGB-guidance module by alternatively concatenating the noisy RAW image with the RGB image, and examine the role of the hyper-

bolic tangent function as the final activation. The results show that the modifications reduce the PSNR from 44.93 to 43.45 and 39.74, respectively.

Sampling Steps. In the next experiment, we examine DDIM [78] for accelerating the sampling process. While DDPM performs T iterations, DDIM reduces the number of sampling steps via a non-Markovian diffusion process. The results in Tab. 7 show that RAW-Diffusion achieves consistent performance with as few as 6 DDIM sampling steps compared to 1000 step DDPM. Reducing the steps to 3 and 2 drops PSNR values for NOD Sony from 39.29 to 38.75 and 36.27, respectively.

Loss Functions. The diffusion model is trained with a combination of mean squared error (\mathcal{L}_{MSE}), L1 (\mathcal{L}_{L1}), and logL1 loss (\mathcal{L}_{logL1}) to learn the reconstruction of the RAW images. In the analysis summarized in Tab. 8, we study the impact of the individual component by progressively adding the losses. On NOD Nikon, the reconstruction quality consistently improves as we add more diverse loss terms. On NOD Sony, the performance across all variants stays comparable, albeit with a minor decrease when training with only \mathcal{L}_{MSE} and \mathcal{L}_{L1} .

RGB-Guidance Backbones. We conduct an analysis of different backbones for the RGB-guidance module, for which, the standard EDSR-based backbone [44] is substituted with RRDB [84] and NAFNet [11] backbones by incorporating the respective feature extraction modules. The results in Tab. 9 demonstrate that the RGB-guidance mod-

Table 6. Impact of the RAW-Diffusion architecture. Our model directly predicts the RAW image, incorporates an RGB-guidance module for conditioning, and a hyperbolic tangent activation.

Experiment	NOD Nikon		NOD Sony	
	PSNR	SSIM	PSNR	SSIM
RAW-Diffusion	44.93	0.983	39.17	0.932
predict noise	5.55	0.001	5.04	0.001
concat RGB	43.45	0.978	38.15	0.920
without TanH	39.74	0.934	36.93	0.850

Table 7. Analysis of the RAW reconstruction performance with a reduced number of sampling steps via DDIM. RAW-Diffusion achieves strong performance with very few sampling steps.

	Timesteps	NOD Nikon		NOD Sony	
		PSNR	SSIM	PSNR	SSIM
DDPM	1000	44.97	0.982	38.79	0.931
DDIM	1000	45.04	0.983	39.02	0.931
	100	45.05	0.983	39.07	0.931
	48	45.05	0.983	39.12	0.932
	24	44.91	0.983	39.16	0.932
	12	45.11	0.983	39.28	0.932
	6	45.16	0.984	39.29	0.931
	3	44.92	0.980	38.75	0.926
	2	44.19	0.975	36.27	0.902

Table 8. Impact of loss components. The combination of \mathcal{L}_{MSE} , \mathcal{L}_{L1} , and $\mathcal{L}_{\log\text{L1}}$ increases the precision.

\mathcal{L}_{MSE}	\mathcal{L}_{L1}	$\mathcal{L}_{\log\text{L1}}$	NOD Nikon		NOD Sony	
			PSNR	SSIM	PSNR	SSIM
✓			43.10	0.970	39.03	0.936
✓	✓		44.35	0.980	38.85	0.926
✓	✓	✓	44.93	0.983	39.17	0.932

Table 9. Analysis of different RGB-Guidance backbones. RAW-Diffusion works well with different backbones.

Backbone	Size	NOD Nikon		NOD Sony	
		PSNR	SSIM	PSNR	SSIM
EDSR	25M	44.93	0.983	39.17	0.932
RRDB	27M	45.18	0.984	38.95	0.930
NAFNet	81M	44.70	0.982	39.11	0.926

Table 10. Analysis of different conditioning architectures

	ControlNet	T2I-Adapter	StableSR	RAW-Diffusion
PSNR	42.15±0.14	42.13±0.28	44.43±0.18	44.93±0.15
SSIM	0.973±0.00	0.969±0.00	0.983±0.00	0.983±0.00

ule achieves robust performance across different backbones. Notably, the most extensive backbone, NAFNet, with a total of 81M parameters, does not enhance the precision further.

RGB-Guidance Conditioning. Next, we provide a comparison of the different conditioning architectures, namely ControlNet [97], T2I-Adapter [59], StableSR [82], and RAW-Diffusion. *ControlNet* uses a simple addition after the first projection layer without sophisticated injection mechanism. *T2I-Adapter* uses a downsampling encoder (which performed worse in our tests) and adds features only within the encoder. *StableSR* uses a time-aware embedding encoder with downsampling (our time-independent encoder is more efficient). The injection is different, modulating only the features before the residual connection, showing reduced performance in our preliminary tests. The experiments are performed using the same training pipeline. The results on NOD Nikon are shown in Tab. 10, demonstrating the superior performance of RAW-Diffusion.

Besides distinctions in conditioning, RAW-Diffusion introduces further general differences, such as loss functions, output activation, RAW-prediction, and a specialized encoder, all essential for detailed RAW image generation.

Dataset Mixing Ratio. Finally, we study the contribution of Cityscapes-RAW and BDD100K-RAW generated by RAW-Diffusion with different mixing ratios. The probability p_{gen} defines the likelihood of sampling a data sample from the generated dataset. The mean performance and standard deviation on NOD Nikon and Sony are shown in Fig. 5. The results of training exclusively on the original images, i.e., $p_{\text{gen}} = 0$, are highlighted by a dashed line.

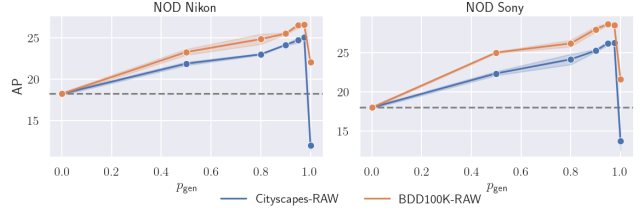


Figure 5. Analysis of different probabilities p_{gen} . The performance improves with increasing probability of sampling from Cityscapes-RAW and BDD100K-RAW, respectively, reaching a peak before training exclusively on the generated datasets.

The experiment reveals that best performance is achieved by training primarily on Cityscapes-RAW and BDD100K-RAW, respectively, complemented with a minor portion of the original image, i.e., p_{gen} of 95% or 97.5%. When $p_{\text{gen}} = 1$, the training is performed on the generated datasets exclusively without any NOD images.

5. Limitations and Future Work

Although our method has proven to be data-efficient, dedicated training for each camera sensor is required. We plan to work on the generalization ability of our method via conditioning for a multi-sensor model. We also emphasize that as a generative model, RAW-Diffusion cannot mitigate any existing biases in the datasets. Metadata is missing for a bias/fairness evaluation. However, we would like to target the removal of dataset bias in our future work. In object detection, images from NOD with overlapping or small objects reveal the limitations of standard models, suggesting the adaptation of specialized models [94, 99].

6. Conclusion

In this work, we presented RAW-Diffusion, a novel diffusion-based method for generating high-fidelity RAW images guided by RGB images. RAW-Diffusion introduces an RGB-guidance module for extracting low-level and high-level guidance features. These features are incorporated into the iterative denoising process via RGB-guided residual blocks to modulate the diffusion features. RAW-Diffusion directly predicts the RAW images and learns the precise reconstruction through iterative denoising. Comprehensive experiments on four DSLR camera datasets show the superior performance of RAW-Diffusion over current state-of-the-art methods. Furthermore, we demonstrate that RAW-Diffusion exhibits remarkable effectiveness, even when trained on a limited dataset with 25 images or fewer. On the downstream task, RAW-Diffusion enables the generation of realistic RAW datasets, like Cityscapes-RAW and BDD100K-RAW, from large-scale RGB datasets, facilitating the training on new camera sensors with very few training samples from the target domain.

References

- [1] Abdelrahman Abdelhamed, Stephen Lin, and Michael S Brown. A high-quality denoising dataset for smartphone cameras. In *Proceedings of the IEEE conference on computer vision and pattern recognition*, pages 1692–1700, 2018.
- [2] Mahmoud Afifi, Abdelrahman Abdelhamed, Abdullah Abuolaim, Abhijith Punnappurath, and Michael S Brown. Cie xyz net: Unprocessing images for low-level computer vision tasks. *IEEE Transactions on Pattern Analysis and Machine Intelligence*, 44(9):4688–4700, 2021.
- [3] Tim Brooks, Ben Mildenhall, Tianfan Xue, Jiawen Chen, Dillon Sharlet, and Jonathan T Barron. Unprocessing images for learned raw denoising. In *Proceedings of the IEEE/CVF Conference on Computer Vision and Pattern Recognition*, pages 11036–11045, 2019.
- [4] Tim Brooks, Ben Mildenhall, Tianfan Xue, Jiawen Chen, Dillon Sharlet, and Jonathan T. Barron. Unprocessing Images for Learned Raw Denoising. In *Proceedings of the IEEE/CVF Conference on Computer Vision and Pattern Recognition*, pages 11036–11045, 2019.
- [5] Mark Buckler, Suren Jayasuriya, and Adrian Sampson. Reconfiguring the imaging pipeline for computer vision. In *Proceedings of the IEEE International Conference on Computer Vision*, pages 975–984, 2017.
- [6] Vladimir Bychkovsky, Sylvain Paris, Eric Chan, and Frédo Durand. Learning photographic global tonal adjustment with a database of input / output image pairs. In *The Twenty-Fourth IEEE Conference on Computer Vision and Pattern Recognition*, 2011.
- [7] Yun-Hao Cao, Hao Yu, and Jianxin Wu. Training Vision Transformers with Only 2040 Images. In *Computer Vision - ECCV 2022*, 2022.
- [8] Nicolas Carion, Francisco Massa, Gabriel Synnaeve, Nicolas Usunier, Alexander Kirillov, and Sergey Zagoruyko. End-to-end object detection with transformers. In Andrea Vedaldi, Horst Bischof, Thomas Brox, and Jan-Michael Frahm, editors, *Computer Vision – ECCV 2020*, pages 213–229, Cham, 2020. Springer International Publishing.
- [9] Ayan Chakrabarti, Daniel Scharstein, and Todd E Zickler. An empirical camera model for internet color vision. In *British Machine Vision Conference*, 2009.
- [10] Ayan Chakrabarti, Ying Xiong, Baochen Sun, Trevor Darrell, Daniel Scharstein, Todd Zickler, and Kate Saenko. Modeling radiometric uncertainty for vision with tone-mapped color images. *IEEE Transactions on Pattern Analysis and Machine Intelligence*, 36(11):2185–2198, 2014.
- [11] Liangyu Chen, Xiaojie Chu, X. Zhang, and Jian Sun. Simple baselines for image restoration. In *European Conference on Computer Vision*, 2022.
- [12] Marcos V Conde, Steven McDonagh, Matteo Maggioni, Ales Leonardis, and Eduardo Pérez-Pellitero. Model-based image signal processors via learnable dictionaries. In *Proceedings of the AAAI Conference on Artificial Intelligence*, pages 481–489, 2022.
- [13] Marcos V Conde, Radu Timofte, Yibin Huang, Jingyang Peng, Chang Chen, Cheng Li, Eduardo Pérez-Pellitero, Fenglong Song, Furui Bai, Shuai Liu, and others. Reversed image signal processing and RAW reconstruction. AIM 2022 challenge report. In *Proceedings of the European Conference on Computer Vision Workshops (ECCVW)*, pages 3–26. Springer, 2022.
- [14] Marius Cordts, Mohamed Omran, Sebastian Ramos, Timo Rehfeld, Markus Enzweiler, Rodrigo Benenson, Uwe Franke, Stefan Roth, and Bernt Schiele. The cityscapes dataset for semantic urban scene understanding. In *2016 IEEE Conference on Computer Vision and Pattern Recognition (CVPR)*, 2016.
- [15] Florinel-Alin Croitoru, Vlad Hondru, Radu Tudor Ionescu, and Mubarak Shah. Diffusion models in vision: A survey. *IEEE Transactions on Pattern Analysis and Machine Intelligence*, 2023.
- [16] Rishit Dagli. Diffuseraw: End-to-end generative raw image processing for low-light images. *arXiv preprint arXiv:2402.18575*, 2023.
- [17] Gourav Datta, Zeyu Liu, Zihan Yin, Linyu Sun, Akhilesh R. Jaiswal, and Peter A. Beerel. Enabling ISPless Low-Power Computer Vision. In *2023 IEEE/CVF Winter Conference on Applications of Computer Vision (WACV)*, pages 2429–2438. IEEE, 2023.
- [18] Paul E Debevec and Jitendra Malik. Recovering high dynamic range radiance maps from photographs. In *Seminal Graphics Papers: Pushing the Boundaries, Volume 2*, pages 643–652. Association for Computing Machinery, 2023.
- [19] Prafulla Dhariwal and Alexander Nichol. Diffusion models beat gans on image synthesis. *Advances in neural information processing systems*, 34:8780–8794, 2021.
- [20] Prafulla Dhariwal and Alexander Nichol. Diffusion models beat GANs on image synthesis. In M. Ran-zato, A. Beygelzimer, Y. Dauphin, P.S. Liang, and

- J. Wortman Vaughan, editors, *Advances in Neural Information Processing Systems*, volume 34, pages 8780–8794. Curran Associates, Inc., 2021.
- [21] Xiaoyi Dong, Yu Zhu, Chenghua Li, Peisong Wang, and Jian Cheng. RISPNet: A network for Reversed image signal processing. In *Computer Vision – ECCV 2022 Workshops*, pages 445–457, 2023.
 - [22] Alexey Dosovitskiy, Lucas Beyer, Alexander Kolesnikov, Dirk Weissenborn, Xiaohua Zhai, Thomas Unterthiner, Mostafa Dehghani, Matthias Minderer, Georg Heigold, Sylvain Gelly, Jakob Uszkoreit, and Neil Houlsby. An Image is Worth 16x16 Words: Transformers for Image Recognition at Scale. In *International Conference on Learning Representations*, 2021.
 - [23] Eilertsen, Gabriel, Joel Kronander, Gyorgy Denes, Rafał Mantiuk, and Jonas Unger. HDR image reconstruction from a single exposure using deep CNNs. *ACM Transactions on Graphics (TOG)*, 36(6), 2017.
 - [24] Stefan Elfwing, Eiji Uchibe, and Kenji Doya. Sigmoid-Weighted Linear Units for Neural Network Function Approximation in Reinforcement Learning. *Neural Networks*, 107:3–11, 2018.
 - [25] Haoyang Fang, Boran Han, Shuai Zhang, Su Zhou, Cuixiong Hu, and Wen-Ming Ye. Data augmentation for object detection via controllable diffusion models. In *Proceedings of the IEEE/CVF Winter Conference on Applications of Computer Vision*, pages 1257–1266, 2024.
 - [26] Michaël Gharbi, Gaurav Chaurasia, Sylvain Paris, and Frédo Durand. Deep joint demosaicking and denoising. *ACM Transactions on Graphics (ToG)*, 35(6):1–12, 2016.
 - [27] Ross Girshick, Jeff Donahue, Trevor Darrell, and Jitendra Malik. Rich feature hierarchies for accurate object detection and semantic segmentation. In *Proceedings of the IEEE conference on computer vision and pattern recognition*, pages 580–587, 2014.
 - [28] Michael D Grossberg and Shree K Nayar. Determining the camera response from images: What is knowable? *IEEE Transactions on pattern analysis and machine intelligence*, 25(11):1455–1467, 2003.
 - [29] Kaiming He, Xinlei Chen, Saining Xie, Yanghao Li, Piotr Dollár, and Ross Girshick. Masked Autoencoders Are Scalable Vision Learners. In *2022 IEEE/CVF Conference on Computer Vision and Pattern Recognition (CVPR)*, 2022.
 - [30] Kaiming He, Xiangyu Zhang, Shaoqing Ren, and Jian Sun. Deep Residual Learning for Image Recognition. In *2016 IEEE Conference on Computer Vision and Pattern Recognition (CVPR)*, pages 770–778, June 2016.
 - [31] Dan Hendrycks and Kevin Gimpel. Gaussian Error Linear Units (GELUs). *arXiv preprint arXiv:1606.08415*, 2016.
 - [32] Jonathan Ho, Ajay Jain, and Pieter Abbeel. Denoising diffusion probabilistic models. In H. Larochelle, M. Ranzato, R. Hadsell, M.F. Balcan, and H. Lin, editors, *Advances in Neural Information Processing Systems*, volume 33, pages 6840–6851. Curran Associates, Inc., 2020.
 - [33] Jonathan Ho, Chitwan Saharia, William Chan, David J Fleet, Mohammad Norouzi, and Tim Salimans. Cascaded diffusion models for high fidelity image generation. *The Journal of Machine Learning Research*, 23(1):2249–2281, 2022.
 - [34] Jonathan Ho and Tim Salimans. Classifier-free diffusion guidance. In *NeurIPS 2021 Workshop on Deep Generative Models and Downstream Applications*, 2021.
 - [35] Yang Hong, Kaixuan Wei, Linwei Chen, and Ying Fu. Crafting object detection in very low light. In *British Machine Vision Conference (BMVC)*, 2021.
 - [36] Glenn Jocher, Ayush Chaurasia, and Jing Qiu. Ultralytics YOLOv8. 2023.
 - [37] Amirhossein Kazerooni, Ehsan Khodapanah Aghdam, Moein Heidari, Reza Azad, Mohsen Fayyaz, Ilker Hacihaliloglu, and Dorit Merhof. Diffusion models in medical imaging: A comprehensive survey. *Medical Image Analysis*, 88, 2023.
 - [38] Seon Joo Kim, Hai Ting Lin, Zheng Lu, Sabine Süsstrunk, Stephen Lin, and Michael S Brown. A new in-camera imaging model for color computer vision and its application. *IEEE Transactions on Pattern Analysis and Machine Intelligence*, 34(12):2289–2302, 2012.
 - [39] Zhifeng Kong, Wei Ping, Jiaji Huang, Kexin Zhao, and Bryan Catanzaro. DiffWave: A versatile diffusion model for audio synthesis. In *International Conference on Learning Representations*, 2021.
 - [40] Alex Krizhevsky, Ilya Sutskever, and Geoffrey E. Hinton. ImageNet classification with deep convolutional neural networks. In *Advances in Neural Information Processing Systems*, 2012.
 - [41] Chenyang Lei, Xudong Jiang, and Qifeng Chen. Robust reflection removal with flash-only cues in the wild. *IEEE Transactions on Pattern Analysis and Machine Intelligence*, 2023.
 - [42] Zhihao Li, Ming Lu, Xu Zhang, Xin Feng, M. Salman Asif, and Zhan Ma. Efficient visual com-

- puting with camera RAW snapshots. *IEEE Transactions on Pattern Analysis and Machine Intelligence*, pages 1–18, 2024.
- [43] Zhetong Liang, Jianrui Cai, Zisheng Cao, and Lei Zhang. Cameranet: A two-stage framework for effective camera isp learning. *IEEE Transactions on Image Processing*, 30:2248–2262, 2021.
 - [44] Bee Lim, Sanghyun Son, Heewon Kim, Seungjun Nah, and Kyoung Mu Lee. Enhanced deep residual networks for single image super-resolution. In *The IEEE Conference on Computer Vision and Pattern Recognition (CVPR) Workshops*, 2017.
 - [45] Stephen Lin and Lei Zhang. Determining the radiometric response function from a single grayscale image. In *2005 IEEE Computer Society Conference on Computer Vision and Pattern Recognition (CVPR’05)*, volume 2, pages 66–73. IEEE, 2005.
 - [46] Tsung-Yi Lin, Piotr Dollár, Ross Girshick, Kaiming He, Bharath Hariharan, and Serge Belongie. Feature pyramid networks for object detection. In *Proceedings of the IEEE conference on computer vision and pattern recognition*, pages 2117–2125, 2017.
 - [47] Tsung-Yi Lin, Priya Goyal, Ross Girshick, Kaiming He, and Piotr Dollár. Focal loss for dense object detection. In *Proceedings of the IEEE international conference on computer vision*, pages 2980–2988, 2017.
 - [48] Tsung-Yi Lin, Michael Maire, Serge J. Belongie, James Hays, Pietro Perona, Deva Ramanan, Piotr Dollár, and C. Lawrence Zitnick. Microsoft COCO: Common objects in context. In *European Conference on Computer Vision*, 2014.
 - [49] Shuai Liu, Chaoyu Feng, Xiaotao Wang, Hao Wang, Ran Zhu, Yongqiang Li, and Lei Lei. Deep-flexisp: A three-stage framework for night photography rendering. In *Proceedings of the IEEE/CVF Conference on Computer Vision and Pattern Recognition*, pages 1211–1220, 2022.
 - [50] Shilong Liu, Zhaoyang Zeng, Tianhe Ren, Feng Li, Hao Zhang, Jie Yang, Qing Jiang, Chunyuan Li, Jianwei Yang, Hang Su, Jun Zhu, and Lei Zhang. Grounding DINO: Marrying DINO with Grounded Pre-Training for Open-Set Object Detection. In *Computer Vision – ECCV 2024*, 2024.
 - [51] Wei Liu, Dragomir Anguelov, Dumitru Erhan, Christian Szegedy, Scott Reed, Cheng-Yang Fu, and Alexander C. Berg. SSD: Single shot MultiBox detector. In *Computer Vision – ECCV 2016*, pages 21–37. Springer International Publishing, 2016.
 - [52] Xinman Liu, Xuanchi Ren, and Ziyi Wu. Inverting Image Signal Processing Pipeline with Diffusion Models. Technical report, University of Toronto, 2022.
 - [53] William Ljungbergh, Joakim Johnander, Christoffer Petersson, and Michael Felsberg. Raw or cooked? object detection on raw images. In *Scandinavian Conference on Image Analysis*, pages 374–385. Springer, 2023.
 - [54] Ilya Loshchilov and Frank Hutter. Decoupled weight decay regularization. In *International Conference on Learning Representations*, 2019.
 - [55] Andreas Lugmayr, Martin Danelljan, Andres Romero, Fisher Yu, Radu Timofte, and Luc Van Gool. Repaint: Inpainting using denoising diffusion probabilistic models. In *Proceedings of the IEEE/CVF Conference on Computer Vision and Pattern Recognition*, pages 11461–11471, 2022.
 - [56] Calvin Luo. Understanding diffusion models: A unified perspective. *arXiv preprint arXiv:2208.11970*, 2022.
 - [57] Tomoo Mitsunaga and Shree K Nayar. Radiometric self calibration. In *Proceedings. 1999 IEEE computer society conference on computer vision and pattern recognition (Cat. No PR00149)*, volume 1, pages 374–380. IEEE, 1999.
 - [58] Igor Morawski, Yu-An Chen, Yu-Sheng Lin, Shusil Dangi, Kai He, and Winston H Hsu. GenISP: Neural ISP for low-light machine cognition. In *Proceedings of the IEEE/CVF Conference on Computer Vision and Pattern Recognition*, pages 630–639, 2022.
 - [59] Chong Mou, Xintao Wang, Liangbin Xie, Yanze Wu, Jian Zhang, Zhongang Qi, Ying Shan, and Xiaohu Qie. T2I-Adapter: Learning Adapters to Dig out More Controllable Ability for Text-to-Image Diffusion Models. In *AAAI Conference on Artificial Intelligence (AAAI)*, 2024.
 - [60] Alexander Quinn Nichol and Prafulla Dhariwal. Improved denoising diffusion probabilistic models. In Marina Meila and Tong Zhang, editors, *Proceedings of the 38th International Conference on Machine Learning*, volume 139 of *Proceedings of Machine Learning Research*, pages 8162–8171. PMLR, July 2021.
 - [61] Alexander Quinn Nichol, Prafulla Dhariwal, Aditya Ramesh, Pranav Shyam, Pamela Mishkin, Bob McGrew, Ilya Sutskever, and Mark Chen. GLIDE: Towards photorealistic image generation and editing with text-guided diffusion models. In Kamalika Chaudhuri, Stefanie Jegelka, Le Song, Csaba Szepesvári, Gang Niu, and Sivan Sabato, editors, *International Conference on Machine Learning, ICML 2022*, volume 162 of *Proceedings of Machine Learning Research*, pages 16784–16804. PMLR, 2022.

- [62] Maxime Oquab, Timothée Darcet, Théo Moutakanni, Huy V. Vo, Marc Szafraniec, Vasil Khalidov, Pierre Fernandez, Daniel HAZIZA, Francisco Massa, Alaaeldin El-Nouby, Mido Assran, Nicolas Ballas, Wojciech Galuba, Russell Howes, Po-Yao Huang, Shang-Wen Li, Ishan Misra, Michael Rabbat, Vasu Sharma, Gabriel Synnaeve, Hu Xu, Herve Jegou, Julien Mairal, Patrick Labatut, Armand Joulin, and Piotr Bojanowski. DINOv2: Learning robust visual features without supervision. *Transactions on Machine Learning Research*, 2024.
- [63] Junji Otsuka, Masakazu Yoshimura, and Takeshi Ohashi. Self-Supervised Reversed Image Signal Processing via Reference-Guided Dynamic Parameter Selection. *arXiv preprint arXiv:2303.13916*, 2023.
- [64] Taesung Park, Ming-Yu Liu, Ting-Chun Wang, and Jun-Yan Zhu. Semantic Image Synthesis with Spatially-Adaptive Normalization. In *2019 IEEE/CVF Conference on Computer Vision and Pattern Recognition (CVPR)*, pages 2332–2341, 2019.
- [65] Prajit Ramachandran, Barret Zoph, and Quoc V. Le. Searching for Activation Functions. In *6th International Conference on Learning Representations, ICLR 2018, Workshop Track Proceedings*, 2018.
- [66] Aditya Ramesh, Prafulla Dhariwal, Alex Nichol, Casey Chu, and Mark Chen. Hierarchical text-conditional image generation with clip latents. *arXiv preprint arXiv:2204.06125*, 1(2):3, 2022.
- [67] Joseph Redmon, Santosh Divvala, Ross Girshick, and Ali Farhadi. You only look once: Unified, real-time object detection. In *Proceedings of the IEEE conference on computer vision and pattern recognition*, pages 779–788, 2016.
- [68] Christoph Reinders, Hanno Ackermann, Michael Ying Yang, and Bodo Rosenhahn. Object recognition from very few training examples for enhancing bicycle maps. In *2018 IEEE Intelligent Vehicles Symposium (IV)*, 2018.
- [69] Christoph Reinders, Hanno Ackermann, Michael Ying Yang, and Bodo Rosenhahn. Learning convolutional neural networks for object detection with very little training data. *Multimodal Scene Understanding*, 2019.
- [70] Christoph Reinders, Frederik Schubert, and Bodo Rosenhahn. ChimeraMix: Image classification on small datasets via masked feature mixing. In *Proceedings of the Thirty-First International Joint Conference on Artificial Intelligence (IJCAI)*, 2022.
- [71] Christoph Reinders, Michael Ying Yang, and Bodo Rosenhahn. Two worlds in one network: Fusing deep learning and random forests for classification and object detection. *Volunteered Geographic Information*, 2024.
- [72] Shaoqing Ren, Kaiming He, Ross Girshick, and Jian Sun. Faster R-CNN: Towards real-time object detection with region proposal networks. In C. Cortes, N. Lawrence, D. Lee, M. Sugiyama, and R. Garnett, editors, *Advances in Neural Information Processing Systems*, volume 28. Curran Associates, Inc., 2015.
- [73] Robin Rombach, Andreas Blattmann, Dominik Lorenz, Patrick Esser, and Björn Ommer. High-resolution image synthesis with latent diffusion models. In *Proceedings of the IEEE/CVF conference on computer vision and pattern recognition*, pages 10684–10695, 2022.
- [74] Eli Schwartz, Raja Giryes, and Alex M Bronstein. Deepisp: Toward learning an end-to-end image processing pipeline. *IEEE Transactions on Image Processing*, 28(2):912–923, 2018.
- [75] Pierre Sermanet, David Eigen, Xiang Zhang, Michaël Mathieu, Rob Fergus, and Yann LeCun. Overfeat: Integrated recognition, localization and detection using convolutional networks. *arXiv preprint arXiv:1312.6229*, 2013.
- [76] Boxin Shi, Zhe Wu, Zhipeng Mo, Dinglong Duan, Sai-Kit Yeung, and Ping Tan. A benchmark dataset and evaluation for non-lambertian and uncalibrated photometric stereo. In *Proceedings of the IEEE Conference on Computer Vision and Pattern Recognition*, pages 3707–3716, 2016.
- [77] Jascha Sohl-Dickstein, Eric Weiss, Niru Maheswaranathan, and Surya Ganguli. Deep unsupervised learning using nonequilibrium thermodynamics. In Francis Bach and David Blei, editors, *Proceedings of the 32nd International Conference on Machine Learning*, volume 37 of *Proceedings of Machine Learning Research*, pages 2256–2265. PMLR, 2015.
- [78] Jiaming Song, Chenlin Meng, and Stefano Ermon. Denoising diffusion implicit models. In *International Conference on Learning Representations*, 2021.
- [79] Mingxing Tan, Ruoming Pang, and Quoc V Le. Efficientdet: Scalable and efficient object detection. In *Proceedings of the IEEE/CVF conference on computer vision and pattern recognition*, pages 10781–10790, 2020.
- [80] Zhi Tian, Chunhua Shen, Hao Chen, and Tong He. Fcos: Fully convolutional one-stage object detection. In *Proceedings of the IEEE/CVF international conference on computer vision*, pages 9627–9636, 2019.

- [81] Brandon Trabucco, Kyle Doherty, Max A Gurinas, and Ruslan Salakhutdinov. Effective data augmentation with diffusion models. In *The Twelfth International Conference on Learning Representations*, 2024.
- [82] Jianyi Wang, Zongsheng Yue, Shangchen Zhou, Kelvin CK Chan, and Chen Change Loy. Exploiting diffusion prior for real-world image super-resolution. In *International Journal of Computer Vision*, 2024.
- [83] Weilun Wang, Jianmin Bao, Wengang Zhou, Dongdong Chen, Dong Chen, Lu Yuan, and Houqiang Li. Semantic Image Synthesis via Diffusion Models. *arXiv preprint arXiv:2207.00050*, 2022.
- [84] Xintao Wang, Ke Yu, Shixiang Wu, Jinjin Gu, Yihao Liu, Chao Dong, Yu Qiao, and Chen Change Loy. ESRGAN: Enhanced super-resolution generative adversarial networks. In Laura Leal-Taixé and Stefan Roth, editors, *The European Conference on Computer Vision Workshops (ECCVW)*, 2019.
- [85] Zhou Wang, A.C. Bovik, H.R. Sheikh, and E.P. Simoncelli. Image quality assessment: From error visibility to structural similarity. *IEEE Transactions on Image Processing*, 13(4):600–612, 2004.
- [86] Yuxin Wu and Kaiming He. Group normalization. *International Journal of Computer Vision*, 128:742–755, 2018.
- [87] Menghan Xia, Xueting Liu, and Tien-Tsin Wong. Invertible grayscale. *ACM Transactions on Graphics (SIGGRAPH Asia 2018 issue)*, 37(6):246:1–246:10, Nov. 2018.
- [88] Shaoan Xie, Zhifei Zhang, Zhe Lin, Tobias Hinz, and Kun Zhang. Smartbrush: Text and shape guided object inpainting with diffusion model. In *Proceedings of the IEEE/CVF Conference on Computer Vision and Pattern Recognition*, pages 22428–22437, 2023.
- [89] Yazhou Xing, Zian Qian, and Qifeng Chen. Invertible Image Signal Processing. *2021 IEEE/CVF Conference on Computer Vision and Pattern Recognition (CVPR)*, pages 6283–6292, 2021.
- [90] Minkai Xu, Lantao Yu, Yang Song, Chence Shi, Stefano Ermon, and Jian Tang. GeoDiff: A geometric diffusion model for molecular conformation generation. In *International Conference on Learning Representations*, 2022.
- [91] Masakazu Yoshimura, Junji Otsuka, Atsushi Irie, and Takeshi Ohashi. Dynamicisp: dynamically controlled image signal processor for image recognition. In *Proceedings of the IEEE/CVF International Conference on Computer Vision*, pages 12866–12876, 2023.
- [92] Masakazu Yoshimura, Junji Otsuka, Atsushi Irie, and Takeshi Ohashi. Rawgment: noise-accounted raw augmentation enables recognition in a wide variety of environments. In *Proceedings of the IEEE/CVF Conference on Computer Vision and Pattern Recognition*, pages 14007–14017, 2023.
- [93] Fisher Yu, Haofeng Chen, Xin Wang, Wenqi Xian, Yingying Chen, Fangchen Liu, Vashisht Madhavan, and Trevor Darrell. BDD100K: A diverse driving dataset for heterogeneous multitask learning. *2020 IEEE/CVF Conference on Computer Vision and Pattern Recognition (CVPR)*, pages 2633–2642, 2018.
- [94] Xiang Yuan, Gong Cheng, Kebing Yan, Qinghua Zeng, and Junwei Han. Small object detection via coarse-to-fine proposal generation and imitation learning. In *Proceedings of the IEEE/CVF International Conference on Computer Vision (ICCV)*, pages 6317–6327, 2023.
- [95] Syed Waqas Zamir, Aditya Arora, Salman Khan, Munawar Hayat, Fahad Shahbaz Khan, Ming-Hsuan Yang, and Ling Shao. Cycleisp: Real image restoration via improved data synthesis. In *Proceedings of the IEEE/CVF conference on computer vision and pattern recognition*, pages 2696–2705, 2020.
- [96] Hongyi Zhang, Moustapha Cissé, Yann N. Dauphin, and David Lopez-Paz. Mixup: Beyond Empirical Risk Minimization. In *International Conference on Learning Representations*, 2018.
- [97] L. Zhang, A. Rao, and M. Agrawala. Adding conditional control to text-to-image diffusion models. In *2023 IEEE/CVF International Conference on Computer Vision (ICCV)*, pages 3813–3824, Los Alamitos, CA, USA, Oct. 2023. IEEE Computer Society.
- [98] Xuaner Zhang, Qifeng Chen, Ren Ng, and Vladlen Koltun. Zoom to learn, learn to zoom. In *Proceedings of the IEEE/CVF Conference on Computer Vision and Pattern Recognition*, pages 3762–3770, 2019.
- [99] Anlin Zheng, Yuang Zhang, Xiangyu Zhang, Xiaojuan Qi, and Jian Sun. Progressive end-to-end object detection in crowded scenes. In *Proceedings of the IEEE/CVF Conference on Computer Vision and Pattern Recognition (CVPR)*, pages 857–866, June 2022.
- [100] Zhengxia Zou, Keyan Chen, Zhenwei Shi, Yuhong Guo, and Jieping Ye. Object detection in 20 years: A survey. *Proceedings of the IEEE*, 2023.

RAW-Diffusion: RGB-Guided Diffusion Models for High-Fidelity RAW Image Generation (Supplementary Material)

In the supplementary material, the RAW-Diffusion hyper-parameters and the training details for object detection with Faster R-CNN and YOLOv8 are described. Furthermore, we provide additional quantitative and qualitative results for the RGB2RAW reconstruction and downstream object detection experiments.

A. Hyper-parameters

The hyper-parameters for the training, architecture, and diffusion process of RAW-Diffusion are detailed in Tab. 11. The number of base features is denoted by N_{Features} and the number of groups used in the group normalization is denoted by $N_{\text{Norm.Groups}}$. Further implementation details can be found in the published code: <https://github.com/SonyResearch/RAW-Diffusion>.

B. Object Detection Training Details

The experiments are performed using a Faster R-CNN [72] and YOLOv8 [36]. Faster R-CNN has a ResNet-50 backbone pretrained on ImageNet, and it is trained with RGB and RAW images normalized using the corresponding mean and standard deviation of the dataset. We apply random flip, random resize, and cropping as data augmentation, use an image size of 416×640 , and train the network for 48 epochs. In particular, for YOLOv8, the images are normalized to $[0, 1]$, we use the same size of 416×640 , and the model is finetuned from a COCO [48] pretrained checkpoint for 10 epochs using random flip augmentation. In addition, the RAW images are reduced to three channels by averaging the two green channels.

For the generation of the RAW datasets (Cityscapes-RAW and BDD100K-RAW) from large-scale RGB datasets, SRISP and RAW-Diffusion are trained on the images of the object detection datasets with a limited number of samples. When combining the original NOD images and the generated datasets, p_{gen} is set to 0.95.

C. Qualitative RGB2RAW Results

Additional qualitative RAW reconstruction results are shown in Fig. 6. The comparison includes all methods, i.e., U-Net [13], UPI [4], InvGrayscale [87], InvISP [89], InvISP⁺ [89], ISPLess [17], ISPLess⁺ [17], CycleR2R [42], RISPNet [21], Diffusion [52], SRISP [63], and RAW-Diffusion.

D. Detailed Object Detection Results

In Tab. 12 and Tab. 13, extended object detection results are presented using Faster R-CNN and YOLOv8, respectively. Performance metrics, including AP, AP₅₀, AP₇₅, AP_S, AP_M, and AP_L, are detailed. The experiments evaluate the adaptation performance on the target domain by training on a limited subset of 100 sample from the original NOD, denoted by RGB and RAW, respectively, and the combination with the generated datasets by SRISP and RAW-Diffusion, i.e., Cityscapes-RAW (SRISP), BDD100K-RAW (SRISP), Cityscapes-RAW (ours), and BDD100K-RAW (ours).

Additionally, the zero-shot performance is shown in Tab. 14 and Tab. 15 using Faster R-CNN and YOLOv8, respectively. The models are trained exclusively on the generated RAW datasets and evaluated on the test set of NOD.

E. Qualitative Object Detection Results

In Fig. 7, qualitative results from different object detection models using Faster R-CNN are presented. The models are trained on RGB images, RAW images, or a combination with the generated datasets. The experiment shows the advantages of RAW images compared to RGB images, especially in low-light scenarios. Furthermore, the integration of the generated RAW datasets, i.e., Cityscapes-RAW and BDD100K-RAW generated by SRISP and RAW-Diffusion, improves the precision.

F. Training on RGB datasets for object detection on RAW images

We analyze if object detection performance on RAW images improves by directly adding RGB samples to the original RAW training set instead of adding converted RAW images. The results of this experiment on NOD Nikon with Cityscapes and BDD100K, respectively, are shown in Tab. 16. Adding RGB training samples does not improve object detection performance as much as our generated RAW dataset. This highlights that the quality and distribution of the training dataset are crucial.



Figure 6. Qualitative results on FiveK Canon (top), NOD Nikon (middle), and NOD Sony (bottom). The reconstructed RAW image and the error map are presented for each method. The RAW images are shown with a gamma correction of $1/2.2$ for visualization.

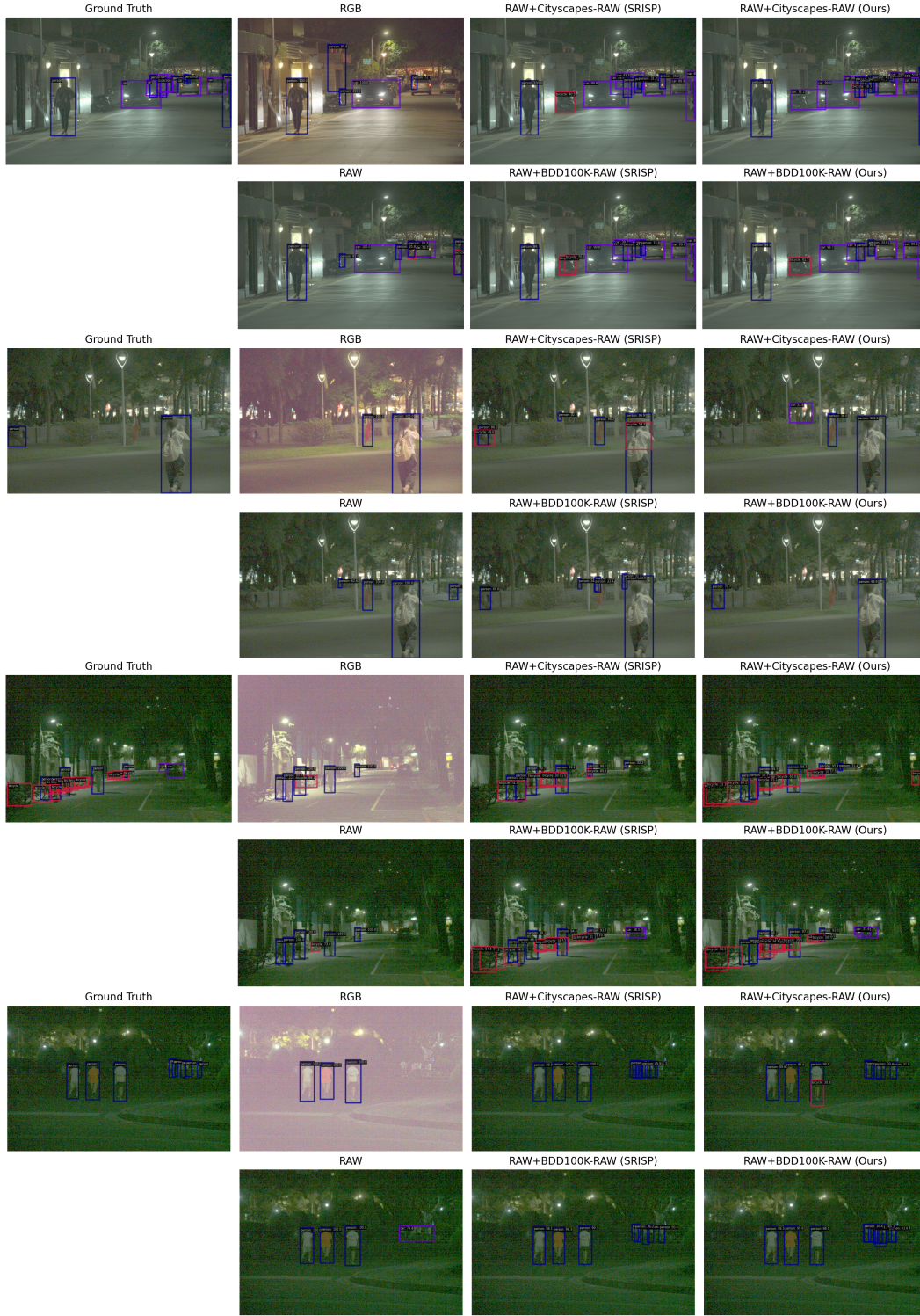


Figure 7. Qualitative object detection results from various models on the test set of NOD Nikon (first and second row) and Sony (third and forth row).

Table 11. Hyper-parameters of RAW-Diffusion.

	Hyper-parameter	Value
Training	Training Steps	70k
	Optimizer	AdamW, $\beta=[0.9, 0.999]$
	Weight Decay	0.0
	Learning Rate	0.0001, linearly decreasing to zero
	Batch Size	4
Architecture	$N_{\text{ResBlocks}}$	2
	N_{Features}	32
	Feature Expansion	(1, 1, 2, 2, 4, 4)
	$N_{\text{Norm,Groups}}$	8
	Attention Block Resolutions	$16 \times 16, 8 \times 8$
	$N_{\text{GM,ResBlocks}}$	4
Diffusion	$C_{\text{GM,Features}}$	64
	Schedule Steps	Linear, $\beta_1 = 0.0001$ to $\beta_T = 0.02$ 1000

Table 12. Object detection results using Faster R-CNN that is trained using 100 NOD training samples (RGB and RAW). Additionally, Cityscapes-RAW and BDD100K-RAW generated by SRISP and RAW-Diffusion are integrated. The best result is shown in bold, and the second best underlined.

Training Dataset	NOD Nikon					
	AP	AP ₅₀	AP ₇₅	AP _S	AP _M	AP _L
RGB	19.1±0.2	36.8±0.4	17.7±0.6	2.0±0.1	16.8±0.4	44.6±0.3
RAW	18.2±0.2	35.3±0.2	17.1±0.2	1.6±0.0	15.9±0.2	43.1±0.3
RAW + Cityscapes-RAW (SRISP)	23.0±0.6	43.9±0.4	21.9±1.5	2.5±0.1	21.4±0.6	49.8±1.4
RAW + BDD100K-RAW (SRISP)	24.2±0.3	45.7±0.4	22.6±0.7	2.9±0.3	21.7±0.3	51.8±1.2
RAW + Cityscapes-RAW (ours)	<u>24.7±0.3</u>	<u>46.3±0.6</u>	<u>23.9±0.2</u>	<u>3.7±0.3</u>	<u>22.8±0.6</u>	<u>52.1±0.9</u>
RAW + BDD100K-RAW (ours)	26.5±0.3	49.3±0.5	25.3±0.5	4.4±0.2	23.9±0.4	54.6±0.6

Training Dataset	NOD Sony					
	AP	AP ₅₀	AP ₇₅	AP _S	AP _M	AP _L
RGB	19.2±0.5	38.2±0.8	17.6±0.5	1.1±0.2	18.4±0.9	38.2±0.6
RAW	18.0±0.1	35.8±0.3	16.3±0.4	1.1±0.3	16.6±0.1	36.8±0.3
RAW + Cityscapes-RAW (SRISP)	23.1±0.4	46.9±0.4	20.0±0.1	2.0±0.2	21.3±1.0	44.4±0.1
RAW + BDD100K-RAW (SRISP)	26.0±0.2	50.5±0.6	24.2±0.5	3.1±0.5	24.4±0.3	46.8±0.6
RAW + Cityscapes-RAW (ours)	<u>26.2±0.3</u>	<u>50.6±0.6</u>	<u>24.9±0.4</u>	<u>3.4±0.5</u>	<u>25.4±0.6</u>	<u>46.9±0.7</u>
RAW + BDD100K-RAW (ours)	28.6±0.1	55.2±0.4	26.4±0.3	4.2±0.1	27.7±0.4	49.6±0.3

Table 13. Object detection results using YOLOv8 evaluating the performance on 100 NOD training samples (RGB and RAW) and the integration of Cityscapes-RAW and BDD100K-RAW generated by SRISP and RAW-Diffusion.

Training Dataset	NOD Nikon					
	AP	AP ₅₀	AP ₇₅	AP _S	AP _M	AP _L
RGB	22.7±1.7	32.9±1.0	22.5±1.8	1.7±0.3	19.6±2.1	55.9±4.1
RAW	25.6±0.2	45.1±0.1	25.6±0.3	2.3±0.1	21.6±0.3	62.4±0.1
RAW + Cityscapes-RAW (SRISP)	29.1±0.1	48.6±0.2	29.4±0.1	3.1±0.1	25.3±0.1	66.0±0.4
RAW + BDD100K-RAW (SRISP)	<u>32.0±0.3</u>	<u>53.1±0.5</u>	<u>32.1±0.4</u>	<u>4.2±0.2</u>	<u>28.6±0.2</u>	<u>68.7±0.5</u>
RAW + Cityscapes-RAW (ours)	29.9±0.3	50.2±0.5	30.7±0.7	3.3±0.1	26.6±0.3	66.4±0.3
RAW + BDD100K-RAW (ours)	32.6±0.1	54.3±0.2	32.6±0.7	4.9±0.1	29.0±0.3	69.2±0.2

Training Dataset	NOD Sony					
	AP	AP ₅₀	AP ₇₅	AP _S	AP _M	AP _L
RGB	18.4±0.3	33.8±0.2	18.4±0.4	1.9±0.0	15.5±2.0	47.3±8.1
RAW	27.6±0.4	49.3±0.2	27.0±0.9	1.6±0.2	23.0±0.1	57.9±0.5
RAW + Cityscapes-RAW (SRISP)	29.5±0.4	51.7±0.6	29.1±0.7	2.9±0.3	25.2±0.2	58.0±1.6
RAW + BDD100K-RAW (SRISP)	<u>32.0±0.7</u>	<u>55.3±0.8</u>	<u>31.6±0.8</u>	<u>3.2±0.0</u>	<u>29.5±0.5</u>	<u>60.0±1.2</u>
RAW + Cityscapes-RAW (ours)	31.0±0.3	54.8±0.5	31.0±0.5	<u>3.2±0.1</u>	27.0±0.3	<u>60.6±0.4</u>
RAW + BDD100K-RAW (ours)	33.6±0.1	58.3±0.2	33.8±0.0	4.2±0.0	31.0±0.1	61.9±0.1

Table 14. Zero-shot object detection results using Faster R-CNN. The models are trained exclusively on the generated datasets and evaluated on the NOD test set.

Training Dataset	NOD Nikon					
	AP	AP ₅₀	AP ₇₅	AP _S	AP _M	AP _L
Cityscapes-RAW (SRISP)	7.7 \pm 1.0	16.8 \pm 2.7	6.4 \pm 0.6	0.4 \pm 0.2	9.5 \pm 0.7	23.8 \pm 1.4
BDD100K-RAW (SRISP)	<u>18.4</u> \pm 0.3	<u>35.9</u> \pm 0.3	<u>15.8</u> \pm 0.5	<u>2.5</u> \pm 0.2	<u>16.7</u> \pm 0.6	<u>38.1</u> \pm 0.2
Cityscapes-RAW (ours)	12.0 \pm 0.7	23.4 \pm 1.6	11.4 \pm 0.5	1.5 \pm 0.4	11.2 \pm 0.7	26.8 \pm 1.7
BDD100K-RAW (ours)	22.0 \pm 0.1	43.1 \pm 0.3	18.8 \pm 0.5	3.5 \pm 0.2	20.8 \pm 0.2	43.4 \pm 0.7

Training Dataset	NOD Sony					
	AP	AP ₅₀	AP ₇₅	AP _S	AP _M	AP _L
Cityscapes-RAW (SRISP)	3.8 \pm 1.1	9.3 \pm 2.8	2.6 \pm 0.5	0.2 \pm 0.1	4.7 \pm 0.6	14.1 \pm 1.7
BDD100K-RAW (SRISP)	<u>16.9</u> \pm 0.6	<u>34.2</u> \pm 0.6	<u>14.5</u> \pm 0.8	<u>.8</u> \pm 0.3	<u>15.6</u> \pm 0.6	<u>30.2</u> \pm 0.9
Cityscapes-RAW (ours)	13.7 \pm 1.3	29.4 \pm 2.3	11.7 \pm 0.8	<u>1.9</u> \pm 0.1	13.5 \pm 1.5	26.5 \pm 2.5
BDD100K-RAW (ours)	21.6 \pm 0.1	43.7 \pm 0.4	18.7 \pm 0.2	3.3 \pm 0.2	20.9 \pm 0.2	37.2 \pm 0.4

Table 15. Zero-shot object detection results using YOLOv8. The models are trained exclusively on the generated datasets and evaluated on the NOD test set.

Training Dataset	NOD Nikon					
	AP	AP ₅₀	AP ₇₅	AP _S	AP _M	AP _L
Cityscapes-RAW (SRISP)	19.1 \pm 0.8	33.5 \pm 1.2	19.0 \pm 0.8	1.7 \pm 0.2	17.2 \pm 0.4	48.9 \pm 2.0
BDD100K-RAW (SRISP)	25.2 \pm 1.2	43.9 \pm 2.6	24.3 \pm 1.1	<u>3.1</u> \pm 0.2	<u>23.9</u> \pm 1.3	53.8 \pm 2.8
Cityscapes-RAW (ours)	<u>25.8</u> \pm 0.7	<u>44.1</u> \pm 0.8	<u>25.7</u> \pm 1.0	2.7 \pm 0.2	23.1 \pm 0.4	<u>58.8</u> \pm 1.9
BDD100K-RAW (ours)	28.8 \pm 0.6	49.8 \pm 0.9	27.6 \pm 0.9	4.3 \pm 0.4	26.8 \pm 0.1	59.9 \pm 2.1

Training Dataset	NOD Sony					
	AP	AP ₅₀	AP ₇₅	AP _S	AP _M	AP _L
Cityscapes-RAW (SRISP)	17.4 \pm 1.0	34.0 \pm 1.3	16.2 \pm 1.6	1.8 \pm 0.1	15.8 \pm 0.6	39.7 \pm 2.3
BDD100K-RAW (SRISP)	24.0 \pm 1.4	43.6 \pm 2.7	23.1 \pm 1.3	2.2 \pm 0.2	22.8 \pm 1.6	45.5 \pm 2.2
Cityscapes-RAW (ours)	<u>26.1</u> \pm 0.5	<u>48.8</u> \pm 0.1	<u>25.0</u> \pm 1.2	<u>2.6</u> \pm 0.1	<u>23.4</u> \pm 0.3	<u>53.6</u> \pm 1.7
BDD100K-RAW (ours)	29.2 \pm 0.6	53.6 \pm 1.0	28.1 \pm 1.1	4.0 \pm 0.3	27.3 \pm 0.4	54.4 \pm 1.9

Table 16. Analysis of integrating the original RGB dataset and our generated RAW dataset. The Average Precision (AP) is shown for each experiment.

Training Dataset	Faster R-CNN	YOLOv8
RAW	18.2 \pm 0.2	25.8 \pm 0.5
RAW + Cityscapes-RGB	23.0 \pm 0.2	26.1 \pm 0.3
RAW + BDD100K-RGB	24.5 \pm 0.3	27.3 \pm 0.3
RAW + Cityscapes-RAW (ours)	24.7 \pm 0.3	29.9 \pm 0.3
RAW + BDD100K-RAW (ours)	26.5 \pm 0.3	32.6 \pm 0.1